

www.acsami.org Research Article

Engineering of Electron Affinity and Interfacial Charge Transfer of Graphene for Self-Powered Nonenzymatic Biosensor Applications

Mohamed Fathi Sanad, Venkata S. N. Chava, Ahmed Esmail Shalan, Lissette Garcia Enriquez, Ting Zheng, Srikanth Pilla, and Sreeprasad T. Sreenivasan*



Cite This: ACS Appl. Mater. Interfaces 2021, 13, 40731-40741



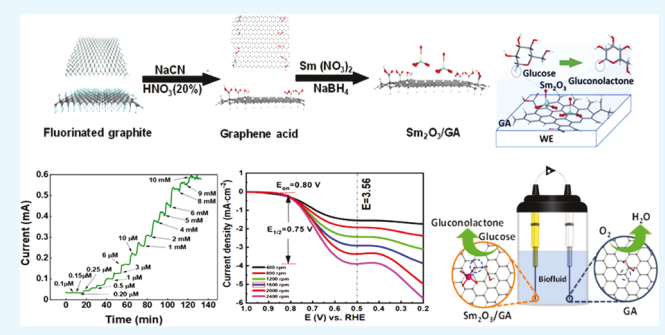
ACCESS I

III Metrics & More

Article Recommendations

supporting Information

ABSTRACT: Facile electron transport and intimate electronic contact at the catalyst—electrode interface are critical for the ideal performance of electrochemical devices such as glucose biofuel cells and biosensors. Here, through a comprehensive experimental—theoretical exploration, we demonstrate that engineering of interfacial properties, including interfacial electron dynamics, electron affinity, electrode—catalyst—adsorbate electrical synergy, and electrocatalytically active surface area, can lead to highly efficient graphene-based electrochemical devices. We selected two closely related but electronically and surface chemically different functionalized graphene analogues—graphene acid (GA) and reduced graphene oxide (rGO)—as the model graphenic plat-



forms. Our studies reveal that compared to rGO, GA is a superior bifunctional catalyst with high oxygen reduction reaction (an onset potential of 0.8 V) and good glucose oxidation activities. Spectroscopic and electrochemical analysis of GA and rGO indicated that the higher carboxylic acid content on GA increases its overall electron affinity and coupled with improved conductivity and band alignment, which leads to GA's better electrochemical performance. The formulation of a heterostructure between GA and samarium oxide (Sm₂O₃) nanoparticles led to augmented conductivity (lower charge-transfer resistance) and glucose binding affinity, resulting in a further enhanced glucose oxidation activity. The interdimensional Sm₂O₃/GA heterostructure, leveraging their enhanced glucose oxidation capacity, exhibited excellent nonenzymatic amperometric glucose sensing performance, with a detection limit of 107 nM and a sensitivity of 20.8 μ A/ μ M. Further, a nonenzymatic, membrane-free glucose biofuel cell (with Sm₂O₃/GA heterostructure as anode and GA as biocathode) produced a power density of 3.2 μ W·cm⁻² (in PBS spiked with 3 mM glucose), which can function as self-powered glucose sensors with 70 nM limit of detection. The study establishes the potential of interfacial engineering of GA to engage it as a highly tunable substrate for a broad range of electrochemical applications, especially in future self-powered biosensors.

KEYWORDS: interfacial engineering, band alignment, graphene acid, rare earth oxide, heterostructure, amperometric sensor, nonenzymatic glucose biofuel cells, self-powered biosensors

1. INTRODUCTION

An efficient power source that can perpetually supply energy is one of the most critical components of implantable bioelectronic devices, including pacemakers, bladder stimulators, and biosensors, to monitor pressure or metabolites. Owing to their biocompatibility and operation at moderate temperatures and near-neutral pH, biofuel cells (BFCs) have emerged as one of the most attractive power sources for implantable biomedical devices. BFCs derive electrical energy by mimicking the biological oxidation of metabolites such as glucose that supply energy for cellular activities. Among various BFCs, because of the abundance of glucose in biological fluids (e.g., saliva), membrane-free glucose biofuel cells (GBFCs) are the front runner as the power source for implantable devices. In GBFCs, the chemical energy is converted to electricity by combining two reactions, namely:

(a) the oxidation of glucose at the anode and (b) the oxygen reduction reaction (ORR) at the cathode. Due to the sluggish glucose oxidation and ORR kinetics in bare electrodes, highly active electrocatalysts at cathode and anode are vital for high-performance GBFCs. Hence, intense research efforts are dedicated to design excellent ORR and glucose oxidation catalysts. The development of glucose oxidation catalysts with superior activity can also help develop high-sensitivity glucose sensors, which own a significant share in the US biosensor

Received: July 1, 2021 Accepted: August 12, 2021 Published: August 23, 2021





market.⁶ Though both enzymatic and nonenzymatic glucose oxidation catalysts are reported, 7,8 owing to their reported inferior device performance (signal variations and lower device stability), enzymatic schemes are generally discouraged for device application. Conversely, nonenzymatic glucose oxidation schemes employing high surface area nanomaterials-based catalysts that can improve the structural uniformity and service life of devices are preferred in GBFCs and biosensors. 10,11

In GBFCs, the efficacy of both cathodic and anodic electrocatalytic reactions at the electrode-catalyst-electrolyte interfaces are controlled by factors, such as the number and density of active sites, electrical conductivity, band alignment, and reaction energy barrier. Moreover, a nonideal design of the interface can lead to slow electron transfer and limited mass transport. Thus, obtaining a synergistically optimized "interface structure" is vital for the superior performance of electrocatalysts and electrochemical devices such as GBFC and biosensors. Nanomaterials in general and low-dimensional nanomaterials (LDNs) like two-dimensional (2D) graphene emerged as highly tunable catalyst platforms to alleviate interfacial mass and charge transport limitations. 12,13 The intense dimensional confinement experienced by LDNs results in the exposure of surface-facet atoms, opening up avenues for the intimate modulation of physicochemical properties through the surface and chemical modifications. For example, surface engineering of LDNs such as inculcation of vacancies is reported to modulate conductivity, adsorption free energy, optimize active sites and reaction kinetics, and derive enhanced electrochemical performance. 14,15 Consequently, graphenic materials are intensely exploited for electrochemical applications.16

Reduced graphene oxide (rGO), due to the high hydrophilicity and conductivity, is the most researched chemically functionalized graphene analogue in electrocatalysts, including the ones in glucose-oxidation-based sensors. 17 However, the presence of various electron-donating (OH) and electronwithdrawing (COOH) functional groups on rGO render them with a mixed affinity toward analytes. 18 While this can be advantageous for the simultaneous detection of analytes with different nucleophilicity, it could be detrimental to selectively anchor electron-rich species such as glucose or oxygen. Hence, the modulation of surface/interface chemical nature to impart increased electron affinity can potentially lead to enhanced electrocatalytic activity of graphenic substrates toward reactions involving electron-rich species. In this direction, recently, a new graphene-derivative called graphene acid (GA) with increased lattice regularity (leading to superior conductivity) and the presence of more electron-withdrawing carboxylic acid groups (approximately 15%) on the basal plane arrived as a viable alternative. ^{19,20} The superior interfacial and lattice properties of GA made it a more appealing platform for electrocatalytic applications such as C-H addition and C-C

Compared to rGO, the increased number of carboxylic acid groups on GA could induce a heightened affinity toward glucose and oxygen. Hence GA, once its interfacial structure is idealized to favor facile interfacial charge transport, could be an ideal GBFC electrode material. Though the applicability of GA for H₂O₂ sensing has been reported, ²² despite its promise, the application of GA in BFCs is unexplored. The construction of heterostructure is one of the most explored pathways to tailor the interfacial properties and catalytic sites.²³ Especially, the combination of 2D materials such as GA with zero-dimensional (0D) nanoparticles are known to create an assemblage of nanoscale heterojunctions that lead to an abundance of active sites and facile charge transport. 24-26 Recently, rare earth oxide (REO) nanoparticles, due to their unique electronic properties emanating from the partially filled forbitals, high work function, and aqueous analyte adoption ability, have gained significant interest as 0D systems with excellent catalytic and promotor properties.²⁷ For example, the surface of light REOs such as samarium oxide (Sm₂O₃) is highly basic and has demonstrated significant promise as photo- and electrocatalysts.²⁸ However, REOs such as Sm₂O₃ (either alone or as heterostructure with LDNs such as graphene) are relatively less explored, especially in fuel cells.²⁹

In this report, leveraging GA and rGO as exemplar graphene substrates, we demonstrate that tuning the properties at the catalyst-electrode-adsorbate interfaces can inculcate highly enhanced bifunctional electrocatalytic activity toward nonenzymatic glucose oxidation and ORR. The increased number of COOH groups on GA compared to rGO resulted in a significantly improved ORR activity with an onset potential of 0.8 V, the highest reported for individual graphenic materials. Further, a novel 0D-2D heterostructure comprising 0D Sm₂O₃ nanoparticles and 2D GA sheets (Sm₂O₃/GA) were prepared through a facile, single-step, in situ reduction process. The constructed Sm₂O₃/GA with tailored band structure and glucose binding affinity depicted a further augmented glucose oxidation activity. Leveraging the superior glucose oxidation activity of the heterostructure, we developed a nonenzymatic, highly sensitive, and selective glucose sensor. Through complementary theoretical studies, we examined and understood the mechanism behind the superior performance of GAbased materials. Finally, using Sm₂O₃/GA as the anode and GA as the cathode, we constructed a GBFC with a power density of 3.2 μ W·cm⁻² (in PBS spiked with 3 mM glucose) and leveraged it for self-powered sensing glucose in biofluids. Our results prove the potential of interfacial engineered GAbased GBFCs as a possible power source for future implantable biomedical devices as well as self-powered biosensors.

2. EXPERIMENTAL SECTION

The details regarding chemical, materials synthesis, and their characterization are included in Supporting Information 1.

2.1. Electrochemical and Biosensing Studies. All of the electrochemical (cyclic voltammetry, linear sweep voltammetry, and chronoamperometry) tests were conducted using a general-purpose three-electrode electrochemical cell setup (CHI potentiostat), where the prepared catalyst material was used as the modified working electrode, the platinum wire as a counter electrode, and Ag/AgCl as a reference electrode. Sulfonated tetrafluoroethylene-based fluoropolymer-copolymer (Nafion) was used as an adhesive polymer to bind the catalyst material with the working electrode. The geometric surface area (A) of the modified working electrodes is 0.071 cm². Chronoamperometric investigations were performed with various concentrations of glucose (100 nM to 10 mM of D-(+)-Glucose solution). For the interference study, during chronoamperometric analysis, interferents (e.g., ascorbic acid and sucrose solutions) were also added sequentially to 0.05 M NaOH solution under constant stirring. The recycling experiments were done for 5000 cycles with the same Sm₂O₃/GA heterostructure-modified electrode in 0.05 M NaOH (pH = 12.7) at ambient conditions in a 25 mL cell. Electrochemical impedance spectroscopy (EIS) measurements were carried out using the same three-electrode workstation in the frequency range of 0.2 Hz-100 kHz at 0.7 V. The EIS spectra were fitted using ZView software.

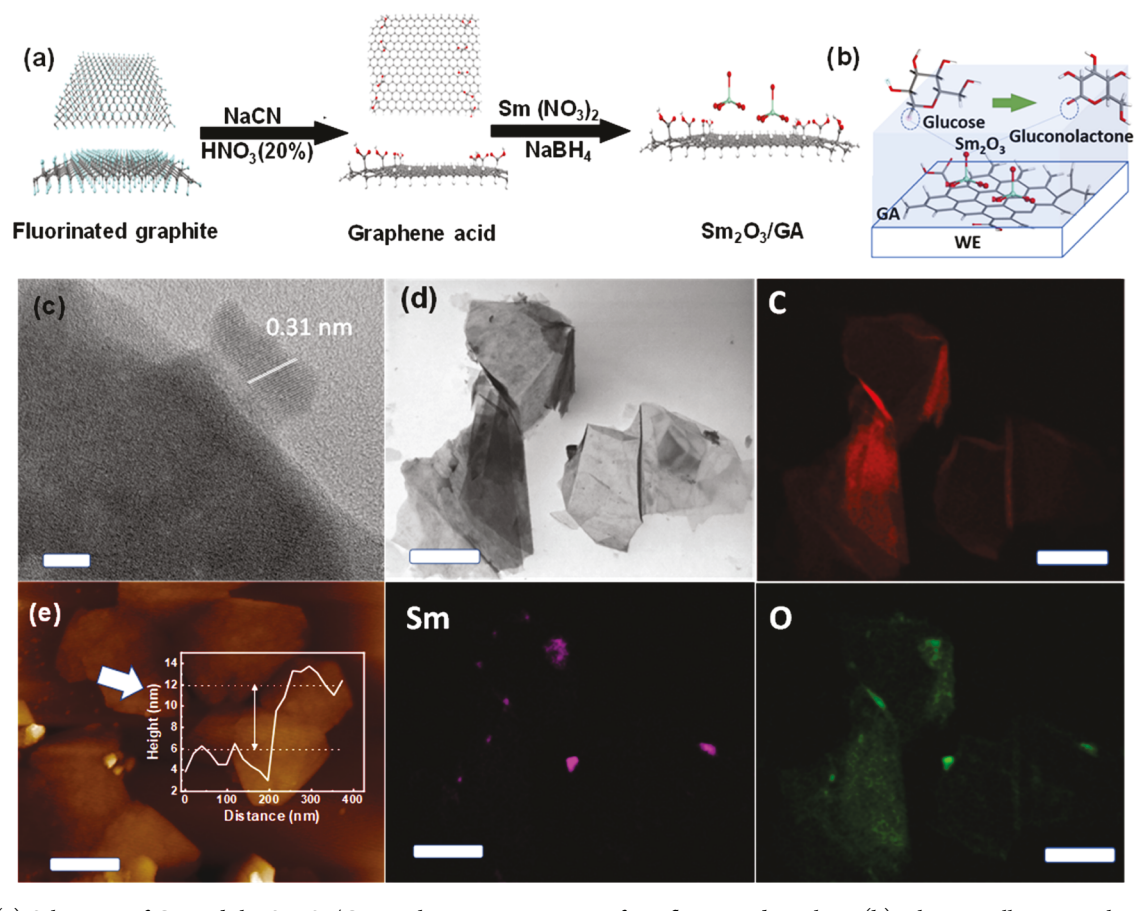


Figure 1. (a) Schematic of GA and the Sm_2O_3/GA synthesis process starting from fluorinated graphite; (b) schematic illustrating the oxidation of glucose to gluconolactone on the Sm_2O_3/GA heterostructure catalyst; (c) HRTEM of the Sm_2O_3/GA heterostructure (scale bar: 5 nm); (d) large area HRTEM image of Sm_2O_3/GA and the corresponding EDS elemental maps showing the presence of carbon, samarium, and oxygen (scale bar: 1 μ m); and (e) AFM topography image of GA sheets (scale bar: 500 nm).

2.2. Oxygen Reduction Reaction Methodology. The oxygen reduction reaction (ORR) measurements were conducted with a three-electrode system using a rotating disk electrode (RDE) connected to an electrochemical workstation (CHI660E, CH Instrument). A 0.05 M of NaOH (pH = 12.7) solution was used as an electrolyte for the oxygen reduction reaction. The working electrode was polished using α -Al₂O₃ and washed with DI water and ethanol using an ultrasonic instrument. Typically, 50 μ g/cm² of the material ink with Nafion was drop-cast onto the working electrode surface. The reference electrode was an AglAgCllKCl standard electrode, and the counter electrode was a carbon graphite rod. All of the LSV measurements were conducted at 1600 r.p.m according to the guidelines of the U.S. Department of Energy protocol.³⁰

2.3. Designing Biofuel Cell and Self-Powered Biosensors. For the BFC electrochemical characterization, cyclic voltammogram at room temperature was recorded in a three-electrode system (CHI potentiostat) using an Ag/AgCl reference electrode, Sm₂O₃/GA heterostructure-modified glassy carbon working electrode, and Pt counter electrode. For the GBFC power density and open-circuit voltage measurements, Sm₂O₃/GA heterostructure-modified glassy carbon electrode and GA were used as the anode and cathode, respectively. Before the measurements, the reaction cell was degassed for about 15 min with Ar gas. Subsequently, the biofluid solution (saliva, Tris-HCL (0.5 M, pH = 7.5), NaOH (0.05 M, pH = 12.7), and PBS (0.1 M, pH = 7), all spiked with glucose) was saturated with oxygen for about 30 min. The power density curves were obtained by measuring the cell voltage versus current. The stability of the biofuel cell was tested by measuring the change in their OCVs values over time.³¹ Discharge curves of the GBFC-based self-powered biosensor were measured by the linear polarization resistance method. According to the polarization curve, the relationship of power output

and the current density was calculated by the formula of P = VI, where I is the current and V is the voltage.

3. RESULTS AND DISCUSSION

3.1. Synthesis and Characterization of Sm₂O₃/GA Heterostructure. Figure 1a shows the preparation of GA and Sm₂O₃/GA. In Sm₂O₃/GA, Sm₂O₃ nanoparticles are anchored on GA sheets via van der Waals (vdW) interactions to create mixed-dimensional (0D-2D) vdW heterostructures with potentially enhanced glucose oxidation capacity (Figure 1b). We conducted detailed structural, morphological, and compositional characterization of the materials using a myriad of microscopic and spectroscopic techniques. The HRTEM and SEM images of Sm₂O₃/GA (Figures 1c and S1) showed GA sheets with embedded darker Sm₂O₃ nanoparticles (with d-spacing 0.31 nm corresponding to the (222) plane of Sm₂O₃). The HRTEM analysis indicated that the crystallite size distribution is in the range of 5–10 nm (Figure S2). Since no capping agent was used during the preparation of Sm₂O₃ particles, aggregation was observed in the most heterostructure irrespective of Sm₂O₃ concentrations (Figure S3a-d). However, the extent of aggregation increased for samples with >25 ppm loading (Figure S3), which can potentially impact the electrocatalytic properties of heterostructures with >25 ppm loading. The EDS analysis also suggested the heterostructure formation. The EDS-based elemental maps (Figures 1d and S4) revealed the presence of Sm₂O₃ and the spatial distribution of C, Sm, and O in the heterostructure. The

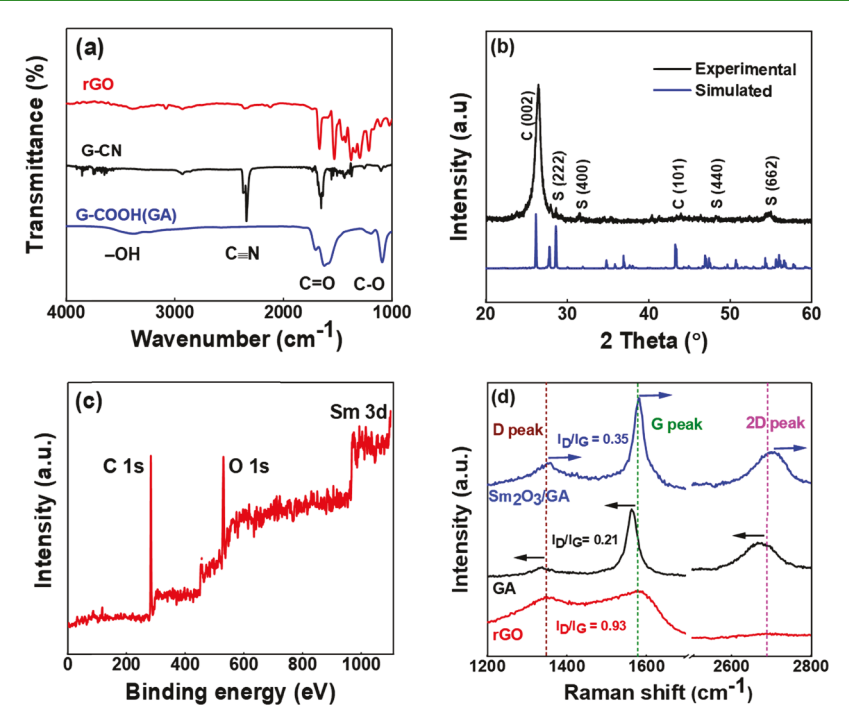


Figure 2. (a) ATR-IR spectrum of the as-prepared rGO, cyano-graphene (G-CN), and GA; (b) experimental and simulated XRD spectrum of Sm₂O₃/GA; (c) XPS survey spectrum of the Sm₂O₃/GA heterostructure; and (d) Raman spectra of rGO, GA, and Sm₂O₃/GA.

one-to-one correspondence between the microscopic image and the EDS maps illustrates heterostructure formation and that darker nanoparticles are composed of Sm₂O₃ and lighter sheets are GA (Figure 1d). The enhanced intensity of O at the exact positions of Sm also indicates that the nanoparticles are Sm₂O₃. An estimated thickness of ~6.5 nm from the AFM topography analysis (Figure 1e) points to the multilayered construct of GA. The ATR-IR (Figure 2a) was employed to characterize GA and rGO formation and the enhanced presence of carboxylic acid on GA. The IR spectrum of GA, in comparison with rGO, displayed an increased absorption at 3350 cm⁻¹ (-OH stretching) and 1725 cm⁻¹ (carbonyl stretching) from the carboxylic acid functionality, indicating successful anchoring of more -COOH. The absence of a 2350 cm⁻¹ feature in GA, unlike the intermediate cyano-graphene (G-CN), confirms the formation of GA.¹⁹ The X-ray diffraction (XRD) of rGO and GA indicated a more ordered lattice in GA than rGO (Figure S5). The XRD spectrum of Sm₂O₃/GA (Figure 2b), in addition to the (002) peak of GA, displayed additional peaks at 28.3, 34.3, 45.3, and 55.6° that can be indexed as (222), (400), (440), and (622) planes of the cubic Sm₂O₃ (JCPDS data No. 42-1461). The experimental XRD spectrum showed a close match to the simulated XRD of Sm_2O_3/GA (Figure 2b).

The heterostructure was analyzed using XPS to unravel the chemical composition of the sample, including the oxidation states of elements and the loading of $\rm Sm_2O_3$ in the heterostructure. The XPS survey spectrum of $\rm Sm_2O_3/GA$ displayed three features corresponding to samarium, oxygen, and carbon (Figure 2c). The high-resolution Sm 3d spectra (Figure S6a) showed Sm $\rm 3d_{3/2}$ (1111.63 eV) and Sm $\rm 3d_{5/2}$ (1083.52 eV) corresponding to Sm in +3 oxidation state as in $\rm Sm_2O_3$, confirming that the nanoparticles seen in the HRTEM image are $\rm Sm_2O_3$. Based on the XPS quantification, $\rm Sm_2O_3$ loading over the heterostructure was found to be close to 7.8% for the 25 ppm $\rm Sm_2O_3/GA$ sample (Figure S6a). The

deconvoluted C 1s spectrum exhibited three components at 284.6, 286.6, and 289 eV, assigned to the C=C, the CO-, and COO- groups (Figure S6b), respectively, suggesting the presence of carboxylic acid moieties on GA. The O 1s spectrum (Figure S6c) also demonstrated features at 531.6 eV (Sm-O), 532 eV (C=O), and 534 eV (-OH) from GA and $\rm Sm_2O_3$. The $\rm Sm_2O_3$ /GA heterostructure formation was also confirmed in our Raman analysis, where we observed features corresponding to both $\rm Sm_2O_3$ (at the spectral range of 150–700 cm⁻¹) and GA (between 1300 and 2800 cm⁻¹) (Figure S7). Hence, XPS, XRD, IR, and Raman analyses established the formation and chemical composition of the $\rm Sm_2O_3$ /GA heterostructure.

Superior electronic properties such as high electron mobility and conductivity are critical for applying graphenic materials in GBFCs. The conductivity of the graphenic matrix is intimately controlled by the sp² carbon content and the sp² domain size. Hence, we explored the sp² content in rGO and GA using XPS (Figure S8). The deconvoluted C 1s spectrum of rGO and GA indicated that the sp² carbon content is higher in GA than rGO (48% in GA to 34.5% in rGO). Further, the XPS analysis also proved that GA possesses more carboxylic acid groups (18%) on its surface compared to rGO (7%). Hence, our XPS results imply that GA retains higher sp² carbon compared to rGO (Figure S8 ad Table S1) through a substantial reduction in functional groups other than carboxylic acids (e.g., -OH groups). Raman spectroscopy can probe structural defects or disorders in graphene and provide insights into its electronic properties, including mobility and doping. 32,33 Figure 2d shows the Raman spectra of rGO, GA, and Sm₂O₃/GA samples, in the spectral range specific to graphene lattice. A prominent G band resulting from the first-order scattering or the E_{2g} vibrational mode of sp² carbons confirmed that all of the samples contain significant sp 2 content. Further, the D band corresponding to $A_{\rm lg}$ breathing mode activated by defects at the Brillouin zone boundary indicates that all of the systems

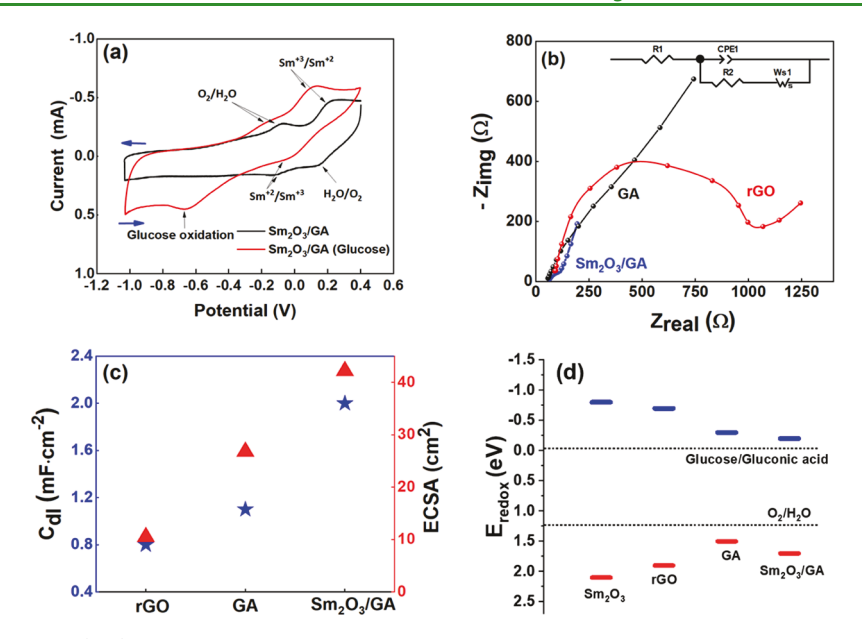


Figure 3. (a) Cyclic voltammetry (CV) response of Sm_2O_3/GA in 0.05 NaOH spiked with 10 Mm glucose, at 100 mV/s scan rate; (b) Nyquist diagram of as-prepared electrocatalysts in an alkaline medium that shows the difference in charge transfer over the prepared electrocatalysts (inset shows the modified Randles circuit used to fit the experimental data); (c) double-layer capacitance and the electrochemical surface area of rGO, GA, and Sm_2O_3/GA catalysts; and (d) HOMO and LUMO levels of as-prepared electrocatalysts.

have defects potentially due to the functional groups. The lattice purity and hence the electrical conductivity of graphene can be correlated with the defect density (estimated from the $I_{\rm D}/I_{\rm G}$). The calculated $I_{\rm D}/I_{\rm G}$ values for rGO, GA, and Sm₂O₃/ GA are 0.96, 0.21, and 0.35, respectively, pointing to the higher conductivity of Sm_2O_3/GA and GA (smaller I_D/I_G values). From the Raman spectrum, we also calculated the crystallite size $(L_{\rm a})$, defect density $(n_{\rm D})$, and interdefect distance $(L_{\rm D})$. The obtained $L_{\rm a}$, $L_{\rm D}$, and $n_{\rm D}$ values for all of the samples are presented in Table S2. The larger crystallite size and longer interdefect distance for GA and Sm₂O₃/GA than rGO again confirm higher carrier mobility (or conductivity) in GA-based samples.³⁶ Further, the D and G peaks of GA and Sm₂O₃/GA displayed a red shift and a blue shift, respectively, compared to the D and G peaks of rGO. These shifts in Raman peaks can be correlated with doping, strain, defects, etc., on graphene. 35 Here, we hypothesize that these peak shifts in GA and Sm₂O₃/GA result from the doping differences in the graphene matrix by functionalization and/or 0D-2D interfacial charge transfer. The red shift of D and G peaks suggests that GA is more p-type than rGO, plausibly due to the presence of a higher number of electron-withdrawing carboxylic groups. Similarly, the blue shift in Sm₂O₃/GA indicates the electron doping in GA through charge transfer from Sm₂O₃ to GA in the heterostructure. Note that a more substantial 2D peak at ~2700 cm⁻¹ in GA and Sm₂O₃/GA samples compared to rGO further confirms the better order of the graphitic lattice and electron dynamics in GA and Sm₂O₃/ GA (supporting our XRD data) (Supporting Information S7). Hence, through XPS and Raman analysis, we conclude that compared to rGO, GA could be a better conducting substrate, whose electronic properties can be controlled further by doping with Sm₂O₃ in the heterostructure. Our currentvoltage (I-V) measurements (Figure S9) confirmed a similar trend in electrical conductivity (σ) , proving the higher electrical conductivity for GA compared to rGO.

3.2. Experimental Electrochemical Evaluation of the **Electrocatalysts.** After confirming the formation of rGO, GA, and Sm₂O₃/GA heterostructure electrocatalysts, we conducted a detailed electrochemical investigation to understand their efficacy as anode and cathode in GBFCs. First, we investigated the electrochemical glucose oxidation performance of Sm₂O₃/ GA and compared it with rGO and GA. To evaluate and compare the preliminary responses of the catalysts to glucose, we analyzed the samples using cyclic voltammetry (CV) in the presence and absence of glucose (Figure 3a). In the absence of glucose, Sm₂O₃/GA-modified electrodes demonstrated welldefined redox peaks at -0.1, -0.01, 0.14, and 0.21 V that correspond to O_2/H_2O , Sm^{+2}/Sm^{+3} , H_2O/O_2 , and Sm^{+3}/Sm^{+2} redox peaks.³⁷ Interestingly, in the presence of glucose, the Sm₂O₃/GA-modified electrode displayed a new redox peak at -0.62 V, which can be reasonably associated with the oxidation of glucose to form gluconolactone. Also, the peak corresponding to H₂O/O₂ disappeared in the presence of glucose, which could probably be due to thermodynamically more favorable glucose oxidation reaction happening in the solution compared to oxygen evolution, as previously reported.³⁸ As shown in Figure S10, all three catalysts displayed a reduction peak in CV corresponding to gluconolactone formed during glucose oxidation. It is also clear that GA-based electrocatalysts (i.e., both GA and Sm₂O₃/ GA) produced a higher current than pure rGO, which followed the order 0.62 mA $(Sm_2O_3/GA) > 0.38$ mA (GA) at 0.75 V. Among the two GA-based catalysts, Sm₂O₃/GA had the highest activity leading to 0.65 mA current. As hypothesized earlier, the better catalytic performance of both GA and Sm₂O₃/GA than rGO is ascribed to the increased electrophilicity afforded by the higher number of electron-withdrawing carboxylic acid groups on GA as confirmed by XPS analysis (Figure S8 and Table S1).³⁹ Figure S11 shows the variation in peak current as a function of the square root of the scan rate. We could fit the measured response with a straight line (correlation coefficient, $R^2 = 0.99$), indicating a diffusion-

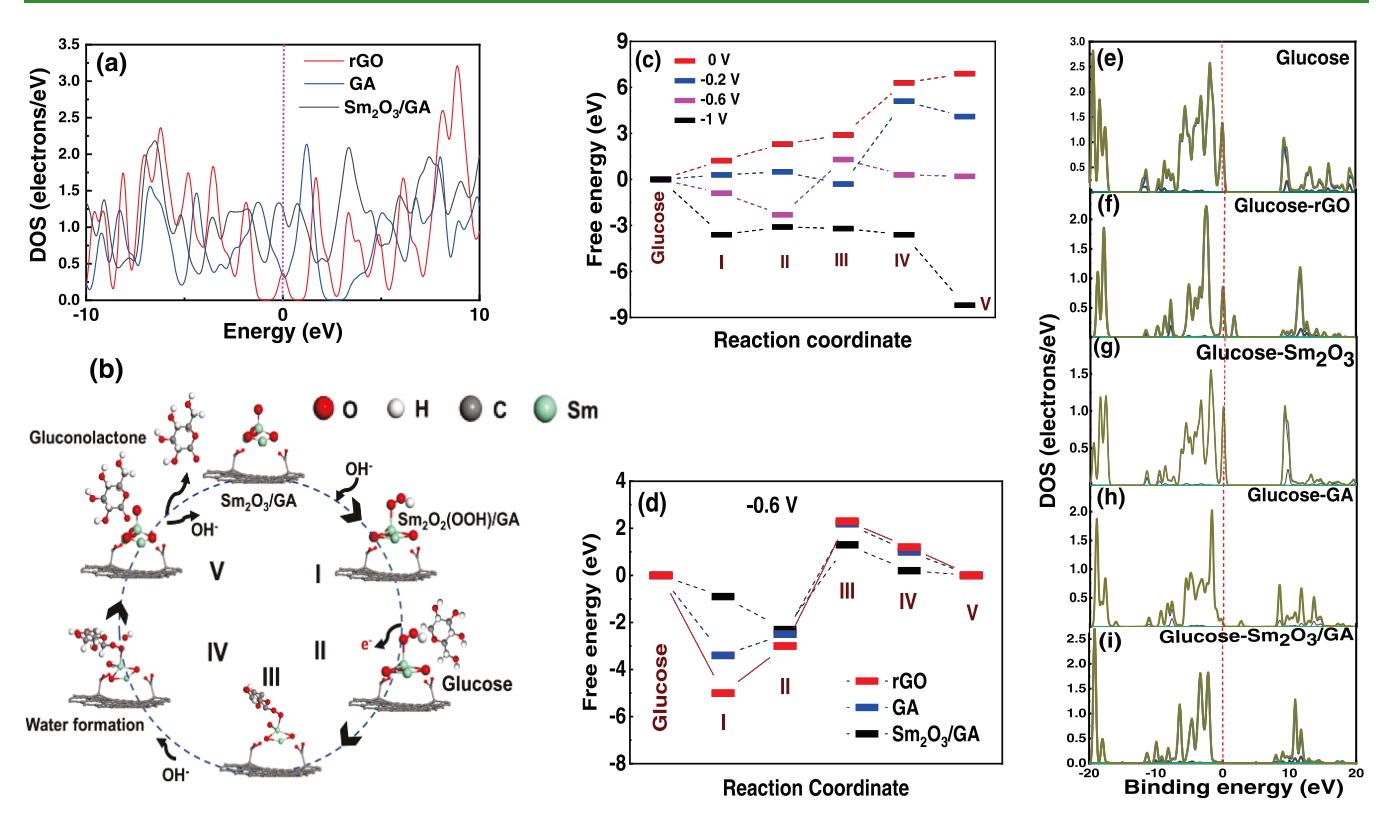


Figure 4. (a) Total density of states of the simulated structures of rGO, GA, and Sm_2O_3/GA ; (b) proposed glucose oxidation mechanism; (c) free-energy diagram at different stages of glucose oxidation over rGO, GA, and Sm_2O_3/GA at -0.6 V; and (d) free-energy change during the glucose oxidation reaction on the Sm_2O_3/GA catalyst when performed at different potentials between 0 and -1 V. (e-i) Partial density of states of oxygen p orbitals in (e) glucose, (f) glucose-rGO, (g) glucose- Sm_2O_3 , (h) glucose-GA, and (i) glucose- Sm_2O_3/GA (dark yellow = sum, blue = P-orbital, and green = S-orbital).

controlled charge transport in the system. 7,40 Also, the restoration of ordered graphite lattice in GA and $\rm Sm_2O_3/GA$ compared to rGO, as evidenced by the Raman, XRD, and XPS investigations, results in faster electron transfer, contributing to the enhanced performance of GA-based catalysts.

Though a clear difference was observed in the CV of the Sm₂O₃/GA catalyst in the presence and absence of glucose indicating the new feature at 0.62 V to be due to the oxidation of glucose, it is also reported that a similar feature can originate from changes in the oxidation state of the metal oxide present in the catalyst. 41 Hence, it is important to confirm the oxidation state of the metal oxide before and after the oxidation. Hence, we analyzed the oxidation state of Sm₂O₃ in the heterostructure before and after the electrocatalytic process using XPS. The XPS analysis (Figure S12) confirmed that Sm remains in +3 oxidation state corresponding to Sm₂O₃, even after the electrocatalytic process. Further, to prove the product of electrocatalytic oxidation of glucose to be gluconolactone, we analyzed the reaction product using ¹³C NMR. A clear shift of the anomeric carbon to a shallow field (182.24 ppm) in the ¹³C NMR pointed to the formation of gluconolactone (Figures S13 and S14). Thus, the apparent variation in the CV in the presence of glucose, XPS-based confirmation of constant oxidation state of Sm₂O₃ before and after glucose oxidation reaction, coupled with the NMR evaluation proving the formation of the gluconolactone, indicate that the new feature at 0.62 V in CV is plausibly due to the oxidation of glucose to gluconolactone. However, a simultaneous reversible redox change of metal oxide catalysts during the glucose oxidation is reported.⁴² Hence, the change in the current density observed

in the CV with the oxidation of glucose might have a contribution from such reversible change in the oxidation state of the metal oxide system in the electrocatalyst. 42,43

The charge-transfer resistance (R_{ct}) is an indicator of conductivity of the substrate and interfacial resistance, critical factors in determining the efficacy of catalyst platforms. Here, we utilized electrochemical impedance spectroscopy (EIS) to estimate the R_{ct} . Figure 3b shows the Nyquist plots of rGO, GA, and Sm₂O₃/GA catalysts obtained from EIS measurements. Figure S15 shows the EIS results of Sm₂O₃/GA samples with different Sm_2O_3 loading (5-30 ppm). While the R_{ct} decreased with an increase in Sm₂O₃ loading from 5 to 25 ppm, beyond 25 ppm of Sm₂O₃ loading, the R_{ct} value of the heterostructure started to increase. Hence, the Sm₂O₃ loading was fixed at 25 ppm in the optimal electrocatalyst sample. The increased R_{ct} of Sm₂O₃/GA above 25 ppm could be due to the clustering of the Sm₂O₃ nanoparticles over GA that causes increased scattering of electrons and decreased electron mobility.⁴⁴ As discussed earlier, the extent of aggregation was significantly higher for samples with >25 ppm loading (Figure S3). Hence, the observed higher particle aggregation might be contributing to the inferior charge-transfer resistance of the catalyst above 25 ppm Sm₂O₃ loading. The Nyquist plots were fitted using a modified Randles equivalent circuit (Inset Figure 3b) to estimate the resistance of the electrolyte solution (R_s) and R_{ct}. The estimated R_{ct} values for rGO, GA, and Sm₂O₃/GA electrodes are 784, 98.33, and 88 Ω , respectively. The other fitted parameters are summarized in Table S4. The comparatively lower R_{ct} of Sm₂O₃/GA modified electrode suggests a highly facile charge transfer that could lead to a

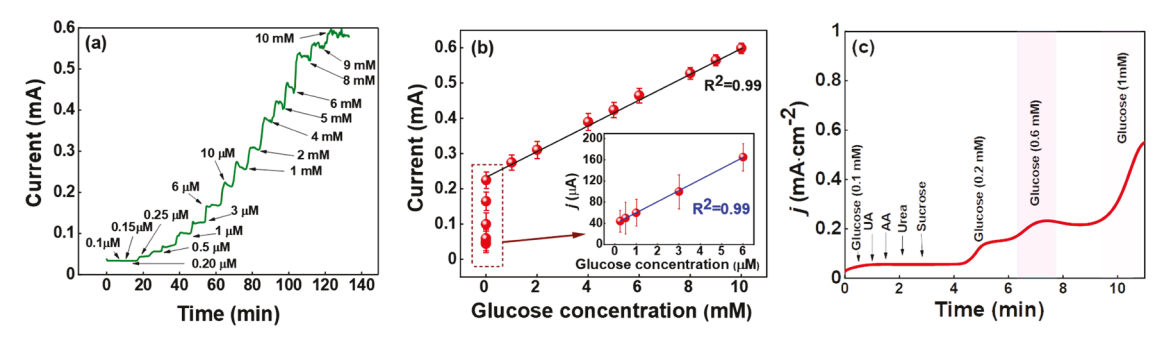


Figure 5. Electrochemical glucose sensing performance of the Sm_2O_3/GA heterostructure. (a) Chronoamperometric response upon sequential addition of glucose solutions; (b) calibration curve of the biosensor with Sm_2O_3/GA as the catalyst. The inset displays the expanded view of the region from 0.1 to 6 μ M; (c) interference study with other blood metabolites present in the system during glucose sensing.

higher Faradic current and more favorable glucose oxidation kinetics for Sm_2O_3/GA compared to GA and rGO.

Construction of heterostructure can lead to synergistic enhancement in electrocatalytic activity by modifying the cumulative electronic structure and creating new catalytic active sites. 23 The creation of newer active sites typically leads to enhanced electrochemically active surface area (ECSA).3 Hence, we estimated the ECSA of Sm₂O₃/GA and compared it with the ECSA of both GA and rGO. The ECSA is calculated as the ratio of double-layer capacitance (C_{dl}) and specific capacitance (C_S) (Figure S16). Since the minimal change was observed in the specific capacitance C_S , the higher C_{dl} values for Sm₂O₃/GA than GA and rGO can be directly correlated with higher ECSA in the heterostructure. The estimated ECSA values are presented in Figure 3d. Additionally, the number of active sites estimated for Sm₂O₃/GA is higher than that of both GA and rGO (Table S5). Finally, we also investigated the electronic properties of catalysts, as they govern the conductivity and redox potentials of catalysts. The formation of heterostructure is known to modify and control the electronic properties of materials such as the band gap, density of states (DOS), etc.⁴⁵ Hence, we electrochemically calculated the HOMO-LUMO levels of as-prepared electrocatalysts (Figure S17).³⁴ Here, the formation of the Sm₂O₃/GA heterostructure reduces the band gap compared to rGO and GA (Figure 3d), indicating the improved electronic conductivity or lower charge-transfer resistance as seen in EIS results. The LUMO of Sm₂O₃/GA is very close to glucose oxidation potential (-0.05 V) compared to rGO or GA. The increased proximity of LUMO level to glucose oxidation potential can also contribute to the higher activity of Sm₂O₃/ GA toward glucose oxidation. On the other hand, the HOMO value of GA is closer to the standard potential of water splitting (1.23 V), suggesting that GA could be a better candidate for ORR and can be used as the cathode in GBFC (discussed in Section 3.5). Hence, our experimental evaluation indicated that a combination of increased electron affinity, conductivity, ECSA, and favorably aligned energy levels leads to the enhanced glucose oxidation capability of the Sm₂O₃/GA heterostructure, compared to GA and rGO.

3.3. DFT-Based Fundamental Exploration of Glucose Oxidation. To gain further fundamental insights into the observed enhanced activity of Sm₂O₃/GA, the surface and electronic properties of catalysts were investigated using DFT. Here, the DOS and the binding affinity (or bond length) of glucose with the catalyst surface were calculated. The calculations indicated that the available DOS near the

Fermi level (when the energy value is close to 0 eV) for Sm_2O_3/GA is higher than GA and rGO (Figure 4a).

The availability of a higher number of states (or DOS) can enhance the activity of Sm₂O₃/GA by facilitating efficient charge transfer between glucose and the catalyst (as indicated in Raman studies). Our energy-based analysis revealed that the most active sites for glucose oxidation in rGO and GA are skeleton carbons near the -COOH functional groups and Sm₂O₃ nanoparticles in Sm₂O₃/GA. While the additional -COOH groups on GA lead to the higher activity of GA than rGO, the extra active sites generated by the presence of Sm₂O₃ in the heterostructure lead to the superior catalytic property of Sm₂O₃/GA. Figure 4b shows the schematic of reaction steps involved in glucose oxidation at the catalyst surface. The corresponding Gibbs free-energy change (ΔG) of each reaction step is shown in Figure 4c. The adsorption of glucose on the catalyst surface was found to be the rate-determining step (Supporting Information S15). The ΔG demonstrated the following trend: $\Delta G_{\text{rGO}} > \Delta G_{\text{GA}} > \Delta G_{\text{Sm},O_3/\text{GA}}$ (Figure 4c). The lower ΔG in Sm₂O₃/GA leads to facile adsorption, which can trigger efficient electron transfer between the glucose intermediate and Sm₂O₃/GA. Thus, the conversion of rGO to GA and the creation of Sm₂O₃/GA could generate an electrondeficient electrocatalytic surface to improve the adsorption of glucose and weaken the adsorption of intermediates, which consequently promotes its glucose oxidation activity. We further calculated the ΔG of Sm₂O₃/GA at different reaction steps as a function of applied potential. The results suggest that V = -0.6 V could be the optimal potential for glucose oxidation as the $\Delta G_{\rm Sm2} {\rm O_3/GA} \sim 0$ at -0.6 V for glucose adsorption (Figure 4d), an excellent match to our CV results where glucose oxidation occurred at V = -0.75 V.

To reveal the variation in glucose affinity to different catalysts explored in the study, we examined the changes in the projected density of states (PDOS) of glucose upon its interaction with the surfaces. Specifically, we calculated the PDOS of S and P orbitals and the total DOS of the oxygen atom in the glucose molecule (Figure 4e–i) before and after it is attached to rGO, $\rm Sm_2O_3$, GA, $\rm Sm_2O_3$ /GA surfaces. Our simulations showed no significant changes in the PDOS of the glucose oxygen atom when it is bound to rGO or $\rm Sm_2O_3$. Conversely, the PDOS or Fermi level ($E_{\rm F}$) exhibited a clear shift when glucose is bound to GA and $\rm Sm_2O_3$ /GA. The $E_{\rm F}$ shift is higher in $\rm Sm_2O_3$ /GA, implying a stronger interaction between $\rm Sm_2O_3$ /GA and glucose. We calculated the length of glucose—catalyst bonds to corroborate this observation, which showed a comparatively shorter bond length when glucose is

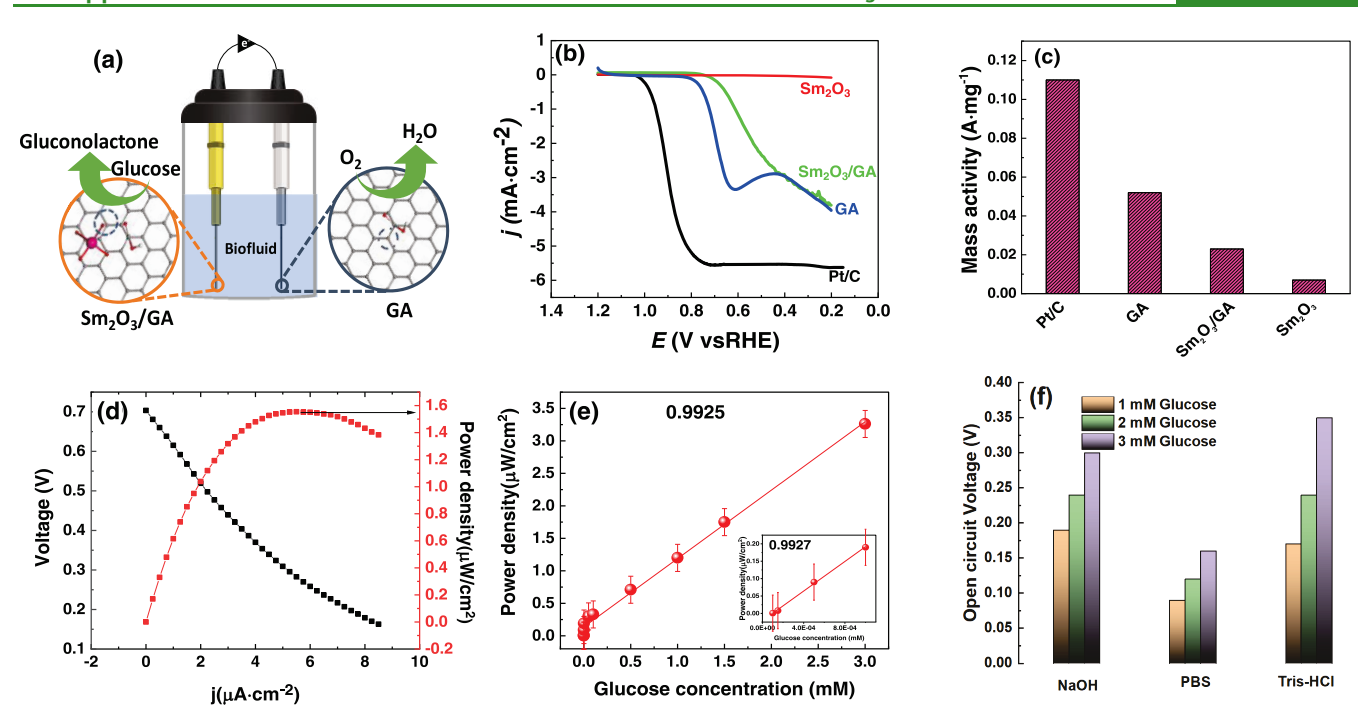


Figure 6. Graphene acid-based glucose biofuel cell; (a) schematic of the GBFC setup, using GA as the cathode for ORR and Sm_2O_3/GA as the anode for glucose oxidation; (b) ORR polarization curves for Pt/C, GA, Sm_2O_3/GA , and Sm_2O_3 at 1600 rpm; (c) ORR mass activity of Pt/C, GA, Sm_2O_3/GA , and Sm_2O_3 catalysts at 0.6 V; (d) power density of the membrane-free GBFC in saliva; (e) calibration plot showing a linear relationship between the power density of the GBFC in response to varying glucose concentrations (0.1 μ M to 3 mM glucose in 0.1 M PBS). Error bars represent the standard deviation of three independent measurements: (f) OCV of the GBFC using Sm_2O_3/GA as the anode, and GA as the cathode in NaOH, PBS, and Tris-HCl electrolytes (1, 2, and 3 mM glucose).

attached to the Sm₂O₃/GA (Figure S18). Similarly, the strong binding of glucose at the catalytic site is also critical for efficient charge transfer or glucose oxidation performance. Hence, we estimated the binding energy of glucose on the catalyst using the following formula: E_b (O-O) = $E(Sm_2O_3/$ GA + Glu) – $E(Sm_2O_3/GA) - E(Glu)$, where $E(Sm_2O_3/GA)$ is the adsorption energy of the heterostructure, E(Glu) is the adsorption energy of the single glucose molecule, and E(Sm₂O₃/GA + Glu) is the adsorption energy of Sm₂O₃/GA heterostructure + glucose system. The calculated binding energy for glucose on the catalysts has the following trend: Sm_2O_3/GA (-7.3 eV) > GA (-6.9 eV) > pure Sm_2O_3 (-6.8 eV) > rGO (-6.7 eV) > Sm_2O_3/rGO (-6.5 eV). The computed negative binding energy of -7.3 eV for Sm₂O₃/GA affirms that glucose binding on the Sm2O3 surface is energetically favored in Sm₂O₃/GA. Hence, our theoretical analysis also provided complementary information about the surface/electronic interactions of glucose with the catalysts, which further validated the experimentally observed superior electrochemical glucose oxidation of Sm₂O₃/GA (Figure S19).

3.4. Sm_2O_3/GA Heterostructure-Based Nonenzymatic Glucose Biosensor. After confirming and understanding the superiority of Sm_2O_3/GA as an efficient electrocatalyst for glucose oxidation, we leveraged the heterostructure to create a highly sensitive, nonenzymatic, amperometric glucose sensor. For this, chronoamperometric (CA) measurements were conducted. Here, the glucose concentration was varied from 100 nM to 10 mM, and the current response (at -0.75 V) at different glucose concentrations was recorded (Figure 5a). A stepwise increase in current with glucose concentration was observed, confirming an accurate glucose electro-oxidation response when GA and Sm_2O_3/GA were employed as the

working electrode. A linear relationship was noted between the current density and glucose concentrations between 250 nM and 10 mM (Figure 5b). Based on the signal-to-noise ratio (S/N) calculation, we estimated a limit of detection (LOD) of 107 nM and a sensitivity of 20.8 μ A/ μ M for glucose sensing for Sm₂O₃/GA.

Though all three materials displayed nearly linear current responses to varying glucose concentrations, Sm₂O₃/GA showed superior performance not only among the three materials explored here but also compared to various other reported nonenzymatic glucose sensors. The sensitivity, linear current response regime, and detection Limits of the Sm₂O₃/ GA are compared to other reported catalysts in Table S6. To test the selectivity of Sm₂O₃/GA, a critical aspect when considered for the practical application, we measured the response of the catalyst to different metabolites to understand how these metabolites can interfere during glucose sensing. Our interference study for the Sm₂O₃/GA system by adding 1 mM of ascorbic acid, sucrose, urea, and uric acid solutions sequentially to 0.1 mM glucose (Figure 5c) indicated only a minor change in current with the addition of other metabolites compared to glucose. The comparatively minor current change against other metabolites confirms the high selectivity of Sm₂O₃/GA toward glucose. The amperometric stability study for the Sm₂O₃/GA-modified electrode in the glucose oxidation reaction showed a stable performance over 25 000 s (Figure S20a) and a highly stable current response over 5000 cycles (Figure S20b), confirming the high-electrochemical stability of Sm₂O₂/GA.

3.5. Glucose Biofuel Cell Studies and Self-Powered Glucose Sensors. Our electrochemical investigations confirmed that Sm_2O_3/GA is an excellent anode material in

GBFCs. The band structure evaluations showed that the HOMO level of GA is closer to the standard oxidation potential of water, suggesting GA could be a promising GBFC cathode. Hence, it might be feasible to construct a membranefree, nonenzymatic GBFC, where the Sm₂O₃/GA-modified glassy carbon electrode is used as the anode for glucose oxidation, and another glassy carbon electrode modified with GA as the ORR cathode (Figure 6a). Our analysis of the ORR performance (Figure 6b) showed that GA has excellent ORR activity with an onset potential of 0.8 V and a half-wave potential of 0.75 V vs RHE. ORR mass activity calculation (Figure 6c) further confirmed that GA has the best ORR activity among the investigated here. The DFT studies predicted three different sites on GA for ORR, which includes C=C (most active), (C-COOH), and (COC) (Figure S21). Also, the idealized structure of GA and free-energy plot of the ORR over three possible positions of the GA were calculated (Figure S21). Hence, our DFT results also pointed out that GA is a suitable ORR catalyst (or GBFC cathode). While the restoration of C=C in GA compared to rGO could be the reason for the higher activity of GA than rGO, the immobilization of Sm2O3 on GA might be masking some of the active sites leading to decreased ORR activity in Sm₂O₃/ GA. We conducted detailed rotating disk electrode (RDE) measurements that can provide information about the number of electrons involved in the ORR process and help to understand the mechanism and the product of the ORR process. The K-L plots obtained from RDE measurements (Figure S22) showed that the number of electrons involved in the ORR in the case of the GA electrocatalyst is close to 3.56 electrons, which confirms that the catalyst favors the fourelectron pathway. Based on the result, we can exclude hydrogen peroxide formation (which is formed through the two-electron mechanism) and conclude that the ORR reaction product catalyzed by GA is water. 47

After confirming the superior catalytic activity of GA and Sm₂O₃/GA catalysts toward ORR and glucose oxidation, we formulated a GBFC with Sm₂O₃/GA as the anode and GA as the cathode. Though we investigated the electrocatalytic performance of the catalysts in 0.05 M NaOH, for the practical utility of the devices, they must function in conditions similar to bodily fluids. Hence, we investigated the capability of the GBFC to work in PBS and Tris-HCl (simulated electrolytes with pH comparable to bodily fluids) and saliva (exemplary bodily fluid), in addition to NaOH, to test the usability of our GBFC in different environments. Figure S23 shows the CV of the GBFC fueled by 30 mL of saliva at a scan rate of 5 mV·s⁻¹. The CV illustrated both the reduction and oxidation peaks related to ORR and glucose oxidation reactions. Figure 6d shows the power output of the GBFC in saliva as a function of current density. In 30 mL of saliva, our self-powered GBFC generated a maximum power density of 1.55 µW·cm⁻² (Figure 6d) with GA as the cathode and 5.4 μ W·cm⁻² with the Pt (ideal ORR catalyst) cathode (Figure S24). Using the calibration curve, we calculated the amount of glucose in the saliva to be ~1.31 mM, which agrees with reported values for glucose concentration in saliva $(0.008-1.77 \times 10^{-3} \text{ M})$, ⁴⁸ illustrating the potential of our self-powered glucose sensor. The calibration curve exhibited a linear relationship between the overall power density and the glucose concentration in the range from 0.1 μ M to 3 mM (R^2 = 0.99) with a LOD of 70 nM and 3.2 μ W·cm⁻² for 3 mM glucose concentration (Figures S25 and 6e). From the calibration curve, we found that the

biosensor has a threshold power density of 0.015 μ W/cm², at which the biosensor begins to produce a measurable output signal in response to glucose present in the solution. Our GBFC system using GA as the cathode also generated a high open-circuit voltage (OCV) ~ 0.6 V in saliva (Figure S26a). The high OCV values and stability (Figures 6f, S26b-d) obtained in PBS, Tris-HCl, and NaOH confirm the utility of our self-powered GBFC for practical glucose biosensing applications. The obtained power density and OCV values with GBFC (in bodily fluids and simulated fluids) are comparable (Table S7) to recently reported membrane-free BFC (including enzymatic GBFC), 10 highlighting the superiority of our anodic and cathodic materials with potential applicability in both membrane-free and membrane-based selfpowered GBFCs.

4. CONCLUSIONS

In summary, we demonstrated an interface engineered Sm₂O₃/ GA heterostructure anode and GA cathode in designing a highperformance, nonenzymatic, membrane-free GBFC and its utility as a self-powered glucose sensor. Through careful tailoring of the chemical-electronic interactions and charge transport properties at the catalysts-electrolyte interface, our GBFCs produced a power density of 1.55 μ W·cm⁻² in saliva. The superior glucose oxidation capacity of the Sm₂O₃/GA heterostructure was understood using a combined experimental and theoretical approach. Our spectroscopic analysis confirmed the increase in the number of electron-withdrawing carboxylic moieties and conductivity in GA, which aids in improving glucose oxidation kinetics. Our studies also proved that the formation of a Sm₂O₃/GA (OD-2D) heterostructure further enhances glucose oxidation due to increased catalytic sites and tuning of electronic properties (e.g., HOMO-LUMO alignment and reduced charge-transfer resistance). The improved ORR activity of GA was also explored theoretically, and the active sites for the ORR process were elucidated. Moreover, the self-powered sensor could detect nanomolar glucose concentrations with an estimated detection limit of 70 nM. Hence, our study demonstrates the importance of balancing the interfacial structure and physicochemical properties of both the catalyst-electrolyte and catalyst-support interfaces. We envision that the biocompatible GA-based nonenzymatic, high-performance GBFC can be attractive for applications such as implantable and self-powered microscale biomedical devices in the future.

ASSOCIATED CONTENT

Supporting Information

The Supporting Information is available free of charge at https://pubs.acs.org/doi/10.1021/acsami.1c12423.

> Experimental details (chemicals, synthesis, and characterization); SEM study; EDS mapping; XRD of reduced graphene oxide(rGO) and graphene acid (GA); XPS study; Raman study; EIS study of Sm₂O₃/GA (different loading ratios); ¹³C NMR; conductivity measurements; electrochemical characterization of glucose oxidation; ECSA study of as-prepared electrocatalysts; HOMO-LUMO calculation using electrochemistry; DFT, Idealized structures and bond length calculations; Glucose oxidation active sites; Catalyst reusability study; Idealized structures and ORR active sites of

graphene acid; and Electrochemical characterization of the GBFC (PDF)

AUTHOR INFORMATION

Corresponding Author

Sreeprasad T. Sreenivasan – Department of Chemistry and Biochemistry, The University of Texas at El Paso, El Paso, Texas 79968, United States; orcid.org/0000-0002-5728-0512; Email: sreenivasan@utep.edu

Authors

- Mohamed Fathi Sanad Department of Chemistry and Biochemistry, The University of Texas at El Paso, El Paso, Texas 79968, United States; Department of Environmental Sciences and Engineering, The University of Texas at El Paso, El Paso, Texas 79968, United States
- Venkata S. N. Chava Department of Chemistry and Biochemistry, The University of Texas at El Paso, El Paso, Texas 79968, United States; o orcid.org/0000-0003-1800-4846
- Ahmed Esmail Shalan BCMaterials-Basque Center for Materials, Applications and Nanostructures, Leioa 48940, Spain; Central Metallurgical Research and Development Institute (CMRDI), Helwan, Cairo 11421, Egypt; orcid.org/0000-0002-3424-1609
- Lissette Garcia Enriquez Department of Chemistry and Biochemistry, The University of Texas at El Paso, El Paso, Texas 79968, United States
- Ting Zheng Department of Automotive Engineering, Clemson University, Greenville, South Carolina 29607, United States; orcid.org/0000-0002-4115-4626
- Srikanth Pilla Department of Automotive Engineering, Clemson University, Greenville, South Carolina 29607, United States; Clemson Composites Centre, Clemson University, Greenville, South Carolina 29607, United States; Department of Materials Science and Engineering and Department of Mechanical Engineering, Clemson University, Clemson, South Carolina 29602, United States; orcid.org/0000-0003-3728-6578

Complete contact information is available at: https://pubs.acs.org/10.1021/acsami.1c12423

Notes

The authors declare no competing financial interest.

ACKNOWLEDGMENTS

This work was supported by the UTEP startup grant, UT STAR's award, and UTEP-URI award. The authors would also like to acknowledge the partial support from DOE grant #DE-FE0031908 and NSF-PREM grant #DMR-1827745. The authors would like to thank Prof. Luis Echegoyen for the engaging discussions and for providing access to some of the characterization systems.

REFERENCES

- (1) Kwon, C. H.; Ko, Y.; Shin, D.; Kwon, M.; Park, J.; Bae, W. K.; Lee, S. W.; Cho, J. High-Power Hybrid Biofuel Cells Using Layer-by-Layer Assembled Glucose Oxidase-Coated Metallic Cotton Fibers. Nat. Commun. 2018, 9, No. 4479.
- (2) Jeerapan, I.; Sempionatto, J. R.; Wang, J. On-Body Bioelectronics: Wearable Biofuel Cells for Bioenergy Harvesting and Self-Powered Biosensing. Adv. Funct. Mater. 2020, 30, No. 1906243.

- (3) Song, Y.; Min, J.; Gao, W. Wearable and Implantable Electronics: Moving Toward Precision Therapy. ACS Nano 2019, 13, 12280-12286.
- (4) Nyein, H. Y. Y.; Gao, W.; Shahpar, Z.; Emaminejad, S.; Challa, S.; Chen, K.; Fahad, H. M.; Tai, L.-C.; Ota, H.; Davis, R. W.; Javey, A. A Wearable Electrochemical Platform for Noninvasive Simultaneous Monitoring of Ca2+ and pH. ACS Nano 2016, 10, 7216-7224.
- (5) Zheng, Q.; Tang, Q.; Wang, Z. L.; Li, Z. Self-Powered Cardiovascular Electronic Devices and Systems. Nat. Rev. Cardiol. **2021**, 18, 7-21.
- (6) Witkowska Nery, E.; Kundys, M.; Jeleń, P. S.; Jönsson-Niedziółka, M. Electrochemical Glucose Sensing: Is There Still Room for Improvement? Anal. Chem. 2016, 88, 11271-11282.
- (7) Bag, S.; Baksi, A.; Nandam, S. H.; Wang, D.; Ye, X.; Ghosh, J.; Pradeep, T.; Hahn, H. Nonenzymatic Glucose Sensing Using Ni60Nb40 Nanoglass. ACS Nano 2020, 14, 5543-5552.
- (8) Li, J.; Lin, X. Glucose Biosensor Based on Immobilization of Glucose Oxidase in poly(o-aminophenol) Film On Polypyrrole-Pt Nanocomposite Modified Glassy Carbon Electrode. Biosens. Bioelectron. 2007, 22, 2898-2905.
- (9) Zebda, A.; Gondran, C.; Le Goff, A.; Holzinger, M.; Cinquin, P.; Cosnier, S. Mediatorless High-Power Glucose Biofuel Cells Based on Compressed Carbon Nanotube-Enzyme Electrodes. Nat. Commun. 2011, 2, No. 370.
- (10) Sehit, E.; Altintas, Z. Significance of Nanomaterials in Electrochemical Glucose Sensors: An Updated Review (2016-2020). Biosens. Bioelectron. 2020, 159, No. 112165.
- (11) Yang, J.; Liang, X.; Cui, L.; Liu, H.; Xie, J.; Liu, W. a Novel Non-Enzymatic Glucose Sensor based on Pt₃Ru1 Alloy Nanoparticles With High Density Of Surface Defects. Biosens. Bioelectron. 2016, 80, 171-174.
- (12) Zhu, C.; Yang, G.; Li, H.; Du, D.; Lin, Y. Electrochemical Sensors And Biosensors Based on Nanomaterials and Nanostructures. Anal. Chem. 2015, 87, 230-249.
- (13) Luo, W.; Zhu, C.; Su, S.; Li, D.; He, Y.; Huang, Q.; Fan, C. Self-Catalyzed, Self-Limiting Growth of Glucose Oxidase-Mimicking Gold Nanoparticles. ACS Nano 2010, 4, 7451-7458.
- (14) Xie, J.; Zhang, J.; Li, S.; Grote, F.; Zhang, X.; Zhang, H.; Wang, R.; Lei, Y.; Pan, B.; Xie, Y. Controllable Disorder Engineering in Oxygen-Incorporated MoS₂ Ultrathin Nanosheets for Efficient Hydrogen Evolution. J. Am. Chem. Soc. 2013, 135, 17881-17888.
- (15) Bao, J.; Zhang, X.; Fan, B.; Zhang, J.; Zhou, M.; Yang, W.; Hu, X.; Wang, H.; Pan, B.; Xie, Y. Ultrathin Spinel-Structured Nanosheets Rich in Oxygen Deficiencies for Enhanced Electrocatalytic Water Oxidation. Angew. Chem., Int. Ed. 2015, 54, 7399-7404.
- (16) Halder, A.; Zhang, M.; Chi, Q. Electroactive and Biocompatible Functionalization of Graphene for the Development of Biosensing Platforms. Biosens. Bioelectron. 2017, 87, 764-771.
- (17) Ziółkowski, R.; Górski, Ł.; Malinowska, E. Carboxylated Graphene as a Sensing Material for Electrochemical uranyl Ion Detection. Sens. Actuators, B 2017, 238, 540-547.
- (18) Bagri, A.; Mattevi, C.; Acik, M.; Chabal, Y. J.; Chhowalla, M.; Shenoy, V. B. Structural Evolution During the Reduction of Chemically Derived Graphene Oxide. Nat. Chem. 2010, 2, 581-587.
- (19) Bakandritsos, A.; Pykal, M.; Błoński, P.; Jakubec, P.; Chronopoulos, D. D.; Poláková, K.; Georgakilas, V.; Čépe, K.; Tomanec, O.; Ranc, V.; Bourlinos, A. B.; Zbořil, R.; Otyepka, M. Cyanographene and Graphene Acid: Emerging Derivatives Enabling High-Yield and Selective Functionalization of Graphene. ACS Nano 2017, 11, 2982-2991.
- (20) Blanco, M.; Mosconi, D.; Otyepka, M.; Medved', M.; Bakandritsos, A.; Agnoli, S.; Granozzi, G. Combined High Degree of Carboxylation and Electronic Conduction in Graphene Acid Sets New Limits for Metal Free Catalysis in Alcohol Oxidation. Chem. Sci. 2019, 10, 9438-9445.
- (21) Reuillard, B.; Blanco, M.; Calvillo, L.; Coutard, N.; Ghedjatti, A.; Chenevier, P.; Agnoli, S.; Otyepka, M.; Granozzi, G.; Artero, V. Noncovalent Integration of a Bioinspired Ni Catalyst to Graphene

- Acid for Reversible Electrocatalytic Hydrogen Oxidation. ACS Appl. Mater. Interfaces 2020, 12, 5805–5811.
- (22) Lenarda, A.; Bakandritsos, A.; Bevilacqua, M.; Tavagnacco, C.; Melchionna, M.; Naldoni, A.; Steklý, T.; Otyepka, M.; Zbořil, R.; Fornasiero, P. Selective Functionalization Blended With Scaffold Conductivity in Graphene Acid Promotes H₂O₂ Electrochemical Sensing. ACS Omega 2019, 4, 19944–19952.
- (23) Puente Santiago, A. R.; He, T.; Eraso, O.; Ahsan, M. A.; Nair, A. N.; Chava, V. S. N.; Zheng, T.; Pilla, S.; Fernandez-Delgado, O.; Du, A.; Sreenivasan, S. T.; Echegoyen, L. Tailoring the Interfacial Interactions of van der Waals 1T-MoS₂/C₆₀ Heterostructures for High-Performance Hydrogen Evolution Reaction Electrocatalysis. *J. Am. Chem. Soc.* **2020**, *142*, 17923–17927.
- (24) Liu, Y.; Weiss, N. O.; Duan, X.; Cheng, H.-C.; Huang, Y.; Duan, X. Van der Waals Heterostructures and Devices. *Nat. Rev. Mater.* **2016**, *1*, No. 16042.
- (25) Geim, A. K.; Grigorieva, I. V. Van der Waals heterostructures. *Nature* **2013**, 499, 419–425.
- (26) Jariwala, D.; Marks, T. J.; Hersam, M. C. Mixed-dimensional van der Waals Heterostructures. *Nat. Mater.* **2017**, *16*, 170–181.
- (27) Sato, S.; Takahashi, R.; Kobune, M.; Gotoh, H. Basic Properties of Rare Earth Oxides. *Appl. Catal., A* **2009**, *356*, 57–63.
- (28) Cheng, Y.; Nan, H.; Li, Q.; Luo, Y.; Chu, K. A Rare-Earth Samarium Oxide Catalyst for Electrocatalytic Nitrogen Reduction to Ammonia. ACS Sustainable Chem. Eng. 2020, 8, 13908–13914.
- (29) Amorebieta, V. T.; Colussi, A. J. Kinetics and Mechanism of the Heterogeneous Oxidation of Ethane and Ethylene on Samarium(III) Oxide. J. Am. Chem. Soc. 1996, 118, 10236–10241.
- (30) Shinozaki, K.; Zack, J. W.; Richards, R. M.; Pivovar, B. S.; Kocha, S. S. Oxygen Reduction Reaction Measurements on Platinum Electrocatalysts Utilizing Rotating Disk Electrode Technique. *J. Electrochem. Soc.* **2015**, *162*, F1144—F1158.
- (31) Li, X.; Feng, Q.; Lu, K.; Huang, J.; Zhang, Y.; Hou, Y.; Qiao, H.; Li, D.; Wei, Q. Encapsulating Enzyme Into Metal-Organic Framework During In-situ Growth on Cellulose Acetate Nanofibers as Self-Powered Glucose Biosensor. *Biosens. Bioelectron.* **2021**, *171*, No. 112690.
- (32) Che, S.; Jasuja, K.; Behura, S. K.; Nguyen, P.; Sreeprasad, T. S.; Berry, V. Retained Carrier-Mobility and Enhanced Plasmonic-Photovoltaics of Graphene via Ring-centered η 6 Functionalization and Nanointerfacing. *Nano Lett.* **2017**, *17*, 4381–4389.
- (33) Deng, S.; Gao, E.; Wang, Y.; Sen, S.; Sreenivasan, S. T.; Behura, S.; Král, P.; Xu, Z.; Berry, V. Confined, Oriented, and Electrically Anisotropic Graphene Wrinkles on Bacteria. *ACS Nano* **2016**, *10*, 8403–8412.
- (34) Nair, A. N.; Chava, V. S. N.; Bose, S.; Zheng, T.; Pilla, S.; Sreenivasan, S. T. In Situ Doping-Enabled Metal and Nonmetal Codoping in Graphene Quantum Dots: Synthesis and Application for Contaminant Sensing. ACS Sustainable Chem. Eng. 2020, 8, 16565–16576.
- (35) Ferrari, A. C.; Basko, D. M. Raman Spectroscopy as a Versatile Tool for Studying the Properties of Graphene. *Nat. Nanotechnol.* **2013**, *8*, 235–246.
- (36) Ferrari, A. C.; Meyer, J. C.; Scardaci, V.; Casiraghi, C.; Lazzeri, M.; Mauri, F.; Piscanec, S.; Jiang, D.; Novoselov, K. S.; Roth, S.; et al. Raman Spectrum of Graphene and Graphene Layers. *Phys. Rev. Lett.* **2006**, *97*, No. 187401.
- (37) He, J.; Qiu, F.; Xu, Q.; An, J.; Qiu, R. A carbon nanofibers—Sm₂O₃ Nanocomposite: A Novel Electrochemical Platform for Simultaneously Detecting Two Isomers of Dihydroxybenzene. *Anal. Methods* **2018**, *10*, 1852–1862.
- (38) Du, P.; Zhang, J.; Liu, Y.; Huang, M. Hydrogen Generation from Catalytic Glucose Oxidation by Fe-based Electrocatalysts. *Electrochem. Commun.* **2017**, 83, 11–15.
- (39) Tu, N. D. K.; Choi, J.; Park, C. R.; Kim, H. Remarkable Conversion Between n- and p-Type Reduced Graphene Oxide on Varying the Thermal Annealing Temperature. *Chem. Mater.* **2015**, 27, 7362–7369.

- (40) Choi, B. G.; Park, H.; Park, T. J.; Yang, M. H.; Kim, J. S.; Jang, S.-Y.; Heo, N. S.; Lee, S. Y.; Kong, J.; Hong, W. H. Solution Chemistry of Self-Assembled Graphene Nanohybrids for High-Performance Flexible Biosensors. *ACS Nano* **2010**, *4*, 2910–2918.
- (41) Ding, Y.; Wang, Y.; Su, L.; Bellagamba, M.; Zhang, H.; Lei, Y. Electrospun Co_3O_4 Nanofibers for Sensitive and Selective Glucose Detection. *Biosens. Bioelectron.* **2010**, *26*, 542–548.
- (42) Amaniampong, P. N.; Trinh, Q. T.; De Oliveira Vigier, K.; Dao, D. Q.; Tran, N. H.; Wang, Y.; Sherburne, M. P.; Jérôme, F. Synergistic Effect of High-Frequency Ultrasound With Cupric Oxide Catalyst Resulting In A Selectivity Switch In Glucose Oxidation Under Argon. *J. Am. Chem. Soc.* **2019**, *141*, 14772–14779.
- (43) Guo, Y.; Liu, J.; Xu, Y.-T.; Zhao, B.; Wang, X.; Fu, X.-Z.; Sun, R.; Wong, C.-P. In Situ Redox Growth of Mesoporous Pd-Cu₂O Nanoheterostructures for Improved Glucose Oxidation Electrocatalysis. *Sci. Bull.* **2019**, *64*, 764–773.
- (44) Liu, H.; Liu, Y.; Zhu, D. Chemical Doping of Graphene. *J. Mater. Chem.* **2011**, 21, 3335–3345.
- (45) Sim, Y.; Kwak, J.; Kim, S.-Y.; Jo, Y.; Kim, S.; Kim, S. Y.; Kim, J. H.; Lee, C.-S.; Jo, J. H.; Kwon, S.-Y. Formation of 3D Graphene—Ni Foam Heterostructures with Enhanced Performance and Durability for Bipolar Plates in a Polymer Electrolyte Membrane Fuel Cell. J. Mater. Chem. A 2018, 6, 1504—1512.
- (46) Ponnusamy, R.; Gangan, A.; Chakraborty, B.; Rout, C. S. Tuning the Pure Monoclinic Phase of WO₃ and WO₃-Ag Nanostructures for Non-Enzymatic Glucose Sensing Application With Theoretical Insight From Electronic Structure Simulations. *J. Appl. Phys.* **2018**, *123*, No. 024701.
- (47) Kulkarni, A.; Siahrostami, S.; Patel, A.; Nørskov, J. K. Understanding Catalytic Activity Trends in the Oxygen Reduction Reaction. *Chem. Rev.* **2018**, *118*, 2302–2312.
- (48) Lee, H.; Hong, Y. J.; Baik, S.; Hyeon, T.; Kim, D.-H. Enzyme-Based Glucose Sensor: From Invasive to Wearable Device. *Adv. Healthcare Mater.* **2018**, *7*, No. 1701150.